ADVANCED FUNCTIONAL MATERIALS
www.afm-journal.de

Improved Thermoelectric Performance of Silver Nanoparticles-Dispersed Bi_2Te_3 Composites Deriving from Hierarchical Two-Phased Heterostructure

Qihao Zhang, Xin Ai, Lianjun Wang, Yanxia Chang, Wei Luo, Wan Jiang,* and Lidong Chen*

A practical and feasible bottom-up chemistry approach is demonstrated to dramatically enhance thermoelectric properties of the Bi_2Te_3 matrix by means of exotically introducing silver nanoparticles (AgNPs) for constructing thermoelectric composites with the hierarchical two-phased heterostructure. By regulating the content of AgNPs and fine-tuning the architecture of nanostructured thermoelectric materials, more heat-carrying phonons covering the broad phonon mean free path distribution range can be scattered. The results show that the uniformly dispersed AgNPs not only effectively suppress the growth of Bi_2Te_3 grains, but also introduce nanoscale precipitates and form new interfaces with the Bi_2Te_3 matrix, resulting in a hierarchical two-phased heterostructure, which causes intense scattering of phonons with multi-scale mean free paths, and therefore significantly reduce the lattice thermal conductivity. Meanwhile, the improved power factor is maintained due to low-energy electron filtering and excellent electrical transport property of Ag itself. Consequently, the maximum ZT is amazingly found to be enhanced by 304% arising from the hierarchical heterostructure when the AgNPs content reaches 2.0 vol%. This study offers an easily scalable and low-cost route to construct a wide range of multiscale hierarchically heterostructured bulk composites with significant enhancement of thermoelectric performance.

1. Introduction

Thermoelectric (TE) materials for achieving the mutual conversion between thermal energy and electric energy have recently attracted increasing interest due to the growing energy demands, concerns over climate change, and depletion of fossil fuel resources. The efficiency of the TE materials is determined by a dimensionless figure of merit ZT, defined as $ZT = (\alpha^2\sigma/\kappa)T$, where α is the Seebeck coefficient, σ is the electric conductivity, κ is the thermal conductivity, and T is the absolute temperature.[1,2] To maximize the ZT value, a high power factor ($\alpha^2\sigma$) and a low κ are essential requirements. Bulk Bi_2Te_3-based materials have by far been considered to be the most suitable TE materials for energy conversion at room temperature because of the intrinsic low thermal conductivity, and the large Seebeck coefficient with relatively high carrier mobility achieved by multiple reasons such as its special band structure, and suitable constituent atomic composition, and therefore, they dominate the industry associated with thermoelectric cooling applications at present.[3,4] However, the ZT values of Bi_2Te_3 still remains low, imposing a limitation on making it a more efficient TE device. Since the theory proved that low-dimensional materials could have higher ZT than their bulk analogs due both to their lower thermal conductivity and to quantum confinement effects,[5] research interest in TE materials has been rekindled, among which constructing nanostructured thermoelectric material is considered a promising way to improve the thermoelectric performance. To date, many advances in improving ZT have been made by a bulk nanostructuring approach.[6–11] Particularly, introducing nanostructure by using high-energy ball milling combined with hot pressing or melt spinning together with spark plasma sintering (SPS) has been reported to enhance the ZT value of *p*-type Bi–Sb–Te alloys to ≈1.4 from 1.0.[12,13] In principle, the nanosized matrix could generate numerous boundaries or interfaces to cause strong scattering of long wavelength phonon arising from the lattice mismatch and the difference of lattice vibration, and therefore result in a marked decrease in the thermal conductivity. Though nanostructures are promising candidates for enhanced TE properties by decreasing the thermal conductivity, yet electrical conductivity is always concurrently deteriorated in those nanostructures, as electrons are also scattered by the grain boundaries. How to coordinate significantly lower thermal conductivity with minimal impact on the electrical conductivity is a tough issue to be addressed.

Q. H. Zhang, X. Ai, Prof. L. J. Wang, Y. X. Chang, Dr. W. Luo, Prof. W. Jiang
State Key Laboratory for Modification of Chemical Fibers and Polymer Materials College of Materials Science and Engineering
Donghua University
Shanghai 201620, P.R. China
E-mail: wanglj@dhu.edu.cn; wanjiang@dhu.edu.cn
Prof. W. Jiang
School of Material Science and Engineering
Jingdezhen Ceramic Institute
Jingdezhen 333000, P.R. China
Prof. L. D. Chen
State Key Laboratory of High Performance Ceramics and Superfine Microstructure
Shanghai Institute of Ceramics
Chinese Academy of Sciences
Shanghai 200050, P.R. China

DOI: 10.1002/adfm.201402663

Afterward, in the wake of the advancement in material synthesis, embedding nanoparticles (particularly metal nanoparticles) with controlled size into bulk matrix has been adopted to TE system for increasing ZT value, based on the concept of "nanoparticle-in-alloy" or metal-semiconductor heterostructures.[14–17] The advantage of incorporating nanoparticles inside thermoelectric materials is not only to reduce the lattice thermal conductivity due to the newly built interfaces scattering of heat-carrying phonons, but also simultaneously enhance the Seebeck coefficient owing to electron energy filtering effect caused by the scattering of electrons on the band bending at the interfaces between nanoinclusions and the semiconductor host. The enhanced Seebeck coefficient could compensate for the reduce in electrical conductivity to some extent, maintaining the power factor as unaffected as possible. Experimentally, there have been several reports on different thermoelectric systems that verify the effectiveness of this approach, but only for suitable combinations of nanoparticles with thermoelectric matrix at appropriate proportion.[18–27] Still and all, nanocomposite structures have been generally prepared by ball milling of nanoparticles as precipitates or microparticles of TE raw materials as the matrix phase,[12,21–24] and yet such processes for fabricating the low-dimensional structures are delicate, expensive, and difficult to scale up for large-scale applications.[28,29] In addition, the inhomogeneous distribution and agglomeration of incorporated nanoparticles in the matrix are reported to impose an limitation on enhancing the thermoelectric performance.[30] Recently, Biswas et al. proposed constructing all-scale hierarchical architectures to scatter heat-carrying phonons across integrated length scales, consequently going beyond nanostructuring and demonstrating a ZT value of 2.2 at 915 K in PbTe-SrTe (4 mol%) doped with 2 mol% Na.[31] The atomic-scale lattice disorder, nanoscale endotaxial precipitates, and mesoscale grain boundaries could jointly lead to extensive phonon scattering on relevant length scales, achieving the maximum reduction in the lattice thermal conductivity and a large enhancement in the thermoelectric performance. Nevertheless, the reported preparation method is top-down, complicated, high energy-consuming, and time-consuming. A key challenge is how to develop a controllable and straightforward synthetic methodology that will integrate multiple phases/compositions with scalar designed physical properties. Given the issues above, we concentrate on seeking a more easily scalable and low-cost route to obtain a homogeneous dispersion of the minor phase into the bulk matrix for constructing hierarchically heterostructured bulk thermoelectric materials with optimized ZT value.

In this work, we report a facile and robust bottom-up chemical route to synthesize thermoelectric materials with hierarchical two-phased heterostructure by exotically introducing silver nanoparticles (AgNPs) into the Bi_2Te_3 matrix, where the Bi_2Te_3 nanopowders are prepared by the surfactant-mediated hydrothermal method and AgNPs are obtained by using polyol reduction of silver nitrate, respectively, followed by ultrasonic-dispersion treatment and spark plasma sintering. It should be noted that theoretical calculations on different thermoelectric materials have shown that important heat carrying phonons generally have a rather wide phonon mean free path (MFP) distribution.[32–36] At a given volume content, the smaller the second phase particles are, the greater concentration of the interface is, which could result in an increase in phonon scattering probability, a decrease in phonon MFP, and therefore a reduced thermal conductivity. However, too small-sized AgNPs may cause properties significantly different from its bulk form. For example, it is reported that AgNPs with size smaller than 35 nm would be molten at a temperature as low as 350 °C, which is the lowest sintering temperature we can use in this work to achieve dense enough samples with good thermoelectric performance.[18,37] One could imagine that AgNPs with size comparable or below 35 nm can rarely survive as the second phase in this work. Therefore, AgNPs with a mean diameter of 60 nm are chosen to be embedded into the Bi_2Te_3 matrix, which is further because such AgNPs have the features of easy preparation and good repeatability. As a result, AgNPs are found not only to inhibit the growth of Bi_2Te_3 grains during the sintering process, but also to homogeneously distribute at the Bi_2Te_3 grain boundaries, introducing nanoscale precipitates, and form new interfaces. The hierarchical two-phased heterostructure within the AgNPs/Bi_2Te_3 thermoelectric composites causes strong scattering of phonons across integrated length scales, significantly reducing the lattice thermal conductivity. More importantly, Ag as a highly conductive particle is favorable to improve the electrical conductivity. Therefore, we could favorably realize the separate tuning of electrical conductivity and thermal conductivity. Compared with pristine bulk Bi_2Te_3, the samples dispersed with AgNPs exhibit decreased thermal conductivities and improved power factors. Consequently, the maximum ZT of the AgNPs-dispersed Bi_2Te_3 composite is found to be more than three times higher than that of the AgNPs-free bulk Bi_2Te_3, when AgNPs content reaches 2.0 vol%.

2. Results and Discussion

2.1. Phase and Microstructures

In this work, Bi_2Te_3 powders and AgNPs were separately synthesized and characterized at first. The XRD pattern for Bi_2Te_3 powders (**Figure 1**a) shows that all diffraction peaks well match with the JCPDS data card no.15–0863, indicating the as-synthesized powders have a single-phase rhombohedral lattice structure (space group of $R\bar{3}m$). There is no special preferential orientation, which means the highly randomness of the Bi_2Te_3 nanopowders. The Bi_2Te_3 powders with a high yield are well agglomerated and possess some flakelike and near-spherical structure according to the field emission scanning electron microscopy (FE-SEM) image, inset of Figure 1a. The size distribution of the Bi_2Te_3 particles is broad, with particle diameter ranging from several nanometers to several hundred nanometers, which could permit the smaller ones to fill the voids among the larger ones, thereby obtaining a hierarchical structure with high density. Figure 1b shows the UV–vis absorption spectra associated with AgNPs. The appearance of three surface plasmon resonance peaks at 445, 386, and 348 nm indicates the formation of AgNPs.[38] In addition, the XRD patern (inset of Figure 1b) confirms the as-synthesized AgNPs have a single-phase face-centered-cubic lattice structure and suggests their high crystallinity. These nanoparticles are basically uniform in

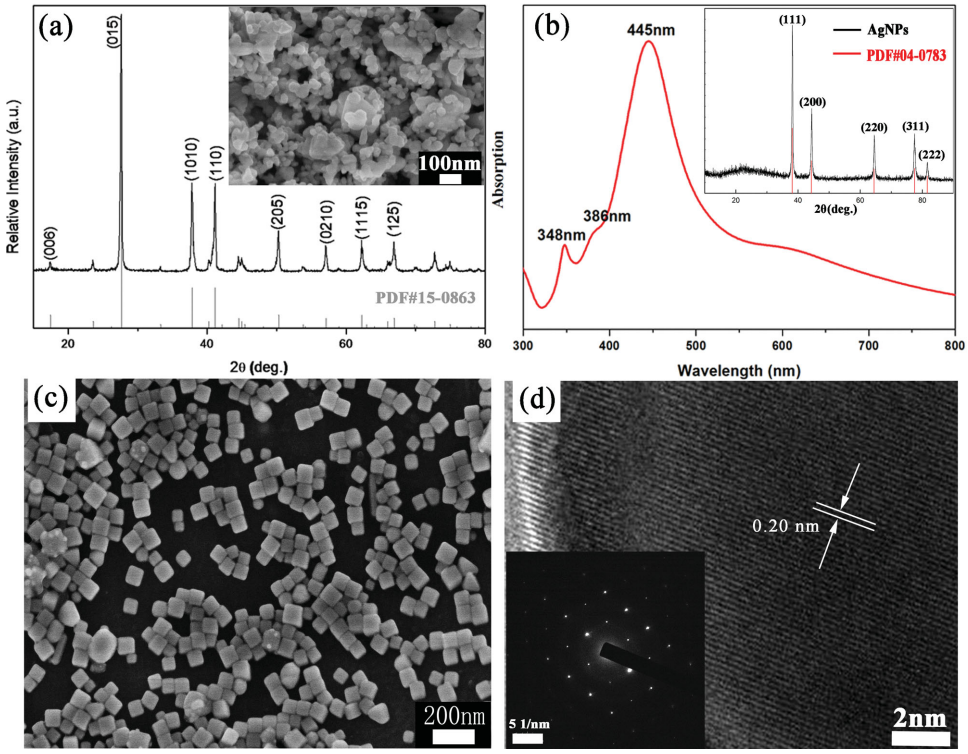

Figure 1. a) XRD pattern and FE-SEM image for the pure Bi_2Te_3 powders, b) UV–vis absorption spectra and XRD pattern, c) FE-SEM image, and d) HRTEM image of AgNPs. The inset in d) shows the selected area electron diffraction pattern of AgNPs.

size and shape and have a mean diameter of 60 nm, as shown in SEM image (Figure 1c). The image also shows the favorable dispersibility and the copiousness in quantity for AgNPs, which indicates we successfully acquire AgNPs using this polyol reduction approach. Figure 1d shows the HRTEM image of one single Ag nanoparticle. The well-resolved lattice fringe with a spacing of 0.20 nm agrees with the interplanar distance between the {200} lattice planes, which is consistent with the previous report.[39] The selected area electron diffraction pattern is shown in the inset of Figure 1d, confirming the formation of single-crystal AgNPs.

Subsequently, the as-synthesized Bi_2Te_3 powders and AgNPs were mixed through the ultrasound and stirring at different proportion. Composite powders were characterized by XRD. As shown in **Figure 2**a, the main diffraction peaks for all composite powders correspond well with the JCPDS data card no.15–0863 for Bi_2Te_3, which means the dispersion of AgNPs has not destroyed the structure of Bi_2Te_3 and the nanopowders have not been oxidized or contaminated during the mixing process. However, no trace of Ag nanoparticles is detected in the compounds due to the small volume fraction of Ag. Figure 2b depicts the XRD patterns of all bulk Bi_2Te_3 with different AgNPs contents prepared by the SPS technique. By comparing the XRD patterns of bulk samples with their corresponding powders, we notice that no peaks about the crystalline phase change, oxidation or impurity is observed, which is attributed to the simple mixing process that is effective to minimize the contamination and relatively short sintering time that minimizes the post-synthetic crystal grain growth of nanoparticles which might otherwise have a detrimental effect on the electronic mobility.[23] Nevertheless, the relative intensities of diffraction peaks for bulk samples have become weaker after sintering, indicating a significant randomness of the grains. It could also be clearly seen in Figure 2c that the three strongest peaks of (015), (1010), and (110) for bulk AgNPs-dispersed Bi_2Te_3 tend to be broadened compared with the one-phase bulk Bi_2Te_3, revealing that the dispersion of AgNPs effectively improves the dispersibility of Bi_2Te_3 matrix and simultaneously suppresses the grain growth to some extent. Furthermore, it should be pointed out that one more weak peak near 30° appears in the XRD patterns of bulk samples, which do not include in the PDF card.15–0863. Because the peak intensity gradually diminishes with increasing AgNPs content, we do not think it was caused by the possibility that Ag was doped in Bi_2Te_3 matrix during the SPS process. By the use of EDX mapping (see Figure 2d), unfortunately, we failed to find a straightforward reason by conducting the compositional analysis.

The fractured surfaces and grain sizes of AgNPs-dispersed Bi_2Te_3 composites after the SPS process were investigated by FE-SEM. **Figure 3** indicates that all sintered samples possess well-crystallized and void-free feature, which is consistent with their high density (as shown in **Table 1**). As seen in Figure 3a, the fractured surface for single-phase bulk Bi_2Te_3 shows a typical anisotropical layered structure without apparent preferential orientation for grains. It is apparent that the grain size of Bi_2Te_3 significantly decreases as AgNPs content increases. Some grains have been unexpectedly reduced to less than 100 nm when AgNPs content reaches 5.0 vol% (Figure 3f), which fully demonstrates that the dispersion of AgNPs effectively suppresses the grains growth of Bi_2Te_3 during the

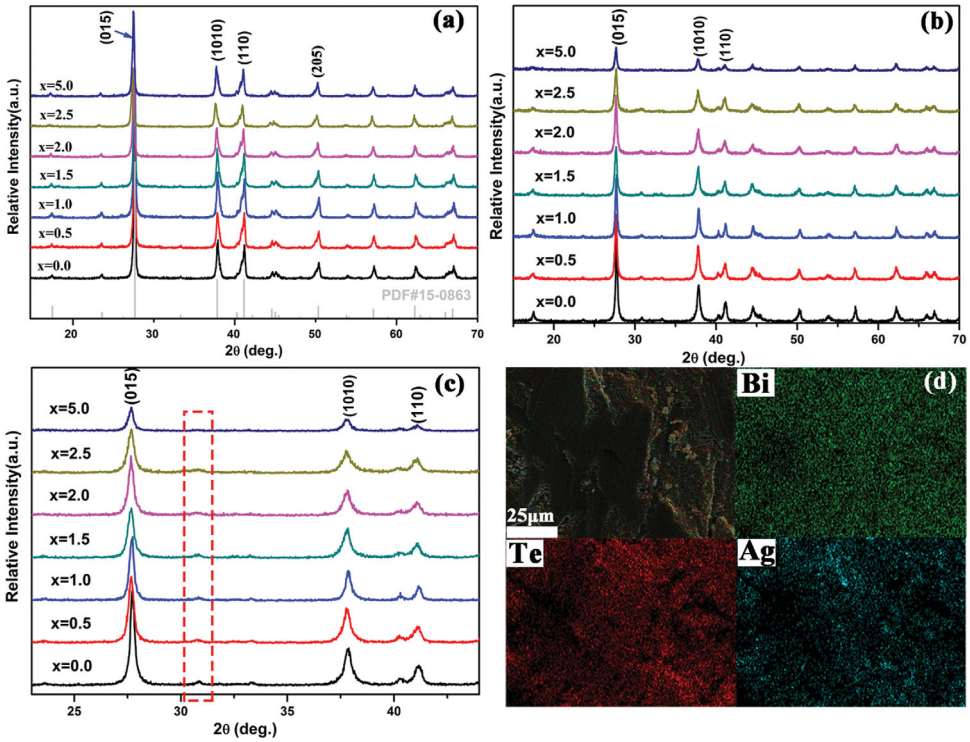

Figure 2. a) Powders XRD patterns of Bi_2Te_3 with *x* vol% AgNPs contents (*x* = 0.0, 0.5, 1.0, 1.5, 2.0, 2.5, 5.0); b) XRD patterns of bulk Bi_2Te_3 with different AgNPs contents; c) XRD patterns of three strongest peaks for bulk AgNPs-dispersed Bi_2Te_3; d) EDX mapping of bulk Bi_2Te_3 with 1.5 vol% AgNPs.

sintering process, resulting in multiscale Bi_2Te_3 grains. The decreased grain size is reported to be beneficial to create a large number of grain boundaries and interfaces that will strongly scatter the long wave phonons and markedly reduce the lattice thermal conductivity.[40–42] The exact hierarchical two-phased heterostructure and composition are subsequently confirmed by the TEM images with EDX patterns.

Detailed microstructure studies by TEM were carried out on bulk Bi_2Te_3 with 5.0 vol% AgNPs. **Figure 4**a presents a low-magnification TEM image confirming the dispersion of AgNPs in the bulk Bi_2Te_3 matrix. The grains of Bi_2Te_3 are closely packed, which is consistent with the high density. The grain boundaries are clearly visible and the observed AgNPs as marked by red arrows are randomly dispersed in the matrix, locating between the grain boundaries. It is quite clear that the grain size of Bi_2Te_3 becomes smaller where AgNPs exist. We assume the smaller ones are beneficial to fill the voids among the larger ones, thereby promoting electrical connectivity at grain boundaries. The inset of Figure 4a is the EDX pattern recorded from the areas marked as A and B, which indicates the chemical composition of the large grain and the nanoparticles at the grain boundary, respectively. Figure 4b is a high-resolution TEM image that depicts the newly built interface between Bi_2Te_3 and AgNPs, as is indicated by a row of yellow dots. The interface is incoherent and rough, which could give rise to higher rates of scattering of the phonons with longer mean free paths, leading to the reduce of lattice thermal conductivity.[43,44] The Bi_2Te_3 grains after sintering process are highly crystalline and mostly nanosized, but the size distribution is broad. Besides large polyhedral grains of hundreds of nanometers in size (Figure 4a), some sphere and platelike Bi_2Te_3 precipitates about 10 nm have been detected as well, as is marked in Figure 4c. Furthermore, the multiscale nanostructure could also be confirmed by FE-SEM images of the fractured surface (Figure 4d), where the grain diameter ranges from dozens to hundreds of nanometers. As expected, the dispersion of AgNPs not only effectively suppresses the growth of Bi_2Te_3 grains to create more grain boundaries, but also forms new interfaces and nanoscale precipitates, resulting in a hierarchical two-phased heterostructure. We believe such a hierarchical two-phased heterostructure that consists of multiscale grains, newly formed interfaces along with the increased grain boundaries will generate intense phonons scattering on broader relevant length scales, significantly reducing the lattice thermal conductivity. It should be noted that in our work, Bi_2Te_3 nanopowders were prepared by the surfactant-mediated hydrothermal method, the size distribution of which was broad, with particle diameter ranging from several nanometers to several hundred nanometers. The AgNPs/Bi_2Te_3 samples were sintered by SPS technique at a heating rate of 70 °C min^{-1}, and at 350 °C for a dwelling time of 6 min. The sintering time was so short that some of Bi_2Te_3 nanoparticles were not fully grown due to the suppression of AgNPs. We cannot rule out the possibility of the existence of Bi–Ag–Te and /or Ag–Te compounds because the size of precipitates is too small to carry out an accurate EDX compositional analysis. Nevertheless, small amount of fine Bi–Ag–Te and /or Ag–Te precipitates, if they do exist, should play a similar role on phonon scattering for

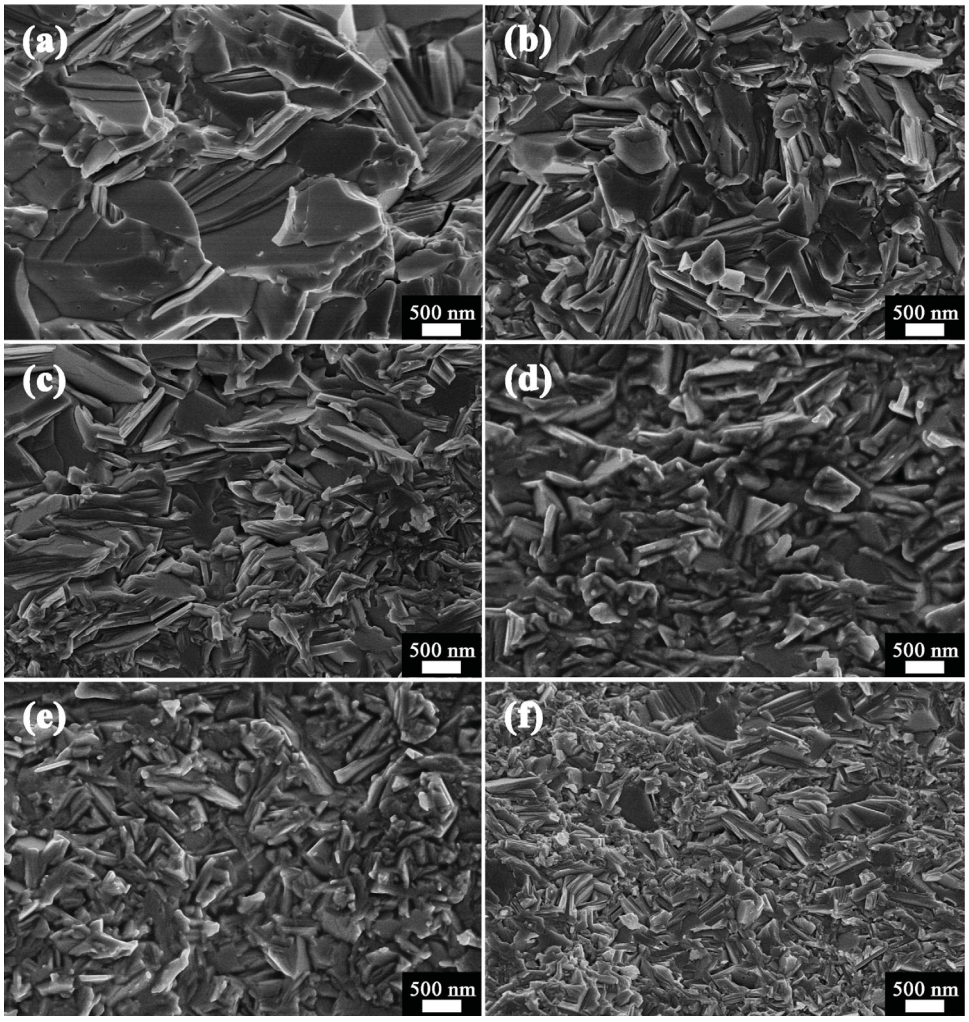

Figure 3. FE-SEM images of the fractured surfaces of AgNPs-dispersed Bi_2Te_3 composites with x vol% AgNPs: a) 0.0 vol%, b) 0.5 vol%, c) 1.0 vol%, d) 1.5 vol%, e) 2.0 vol%, and f) 5.0 vol%.

reducing the lattice thermal conductivity that would further support our main conclusion in this work.

2.2. Thermoelectric Transport Properties

The electrical conductivity (σ), Seebeck coefficient (α), and power factors ($\alpha^2\sigma$) of Bi_2Te_3 bulk samples with different AgNPs contents were measured at temperature ranging from 300 to 475 K and plotted in **Figure 5**. As shown in Figure 5a, all samples show a semiconductor transport behavior that the electrical conductivity increases with increasing measurement temperature, which is similar to some previous reports.[40,45–47] As the AgNPs content increases, the σ values first go up, after achieving a optimum value, the values fall down. As is reported, Ag nanoparticles as a excellent conductor that are dispersed

Table 1. Hall coefficient, carrier concentration, carrier mobility, volume density, and Lorenz number of all bulk samples at 300 K.

Bulk samples Bi_2Te_3+x vol% AgNPs	Volume density [g cm^{-3}]	Hall coefficient [cm^3 C^{-1}]	Carrier concentration [10^{18} cm^{-3}]	Carrier mobility [cm^2 V^{-1} s^{-1}]	Lorenz number [10^{-8} V^2 K^{-2}]
$x = 0.0$	7.788	−3.094	2.02	729.731	1.709
$x = 0.5$	7.772	−2.824	2.21	687.511	1.810
$x = 1.0$	7.783	−1.756	3.56	478.865	1.819
$x = 1.5$	7.828	−1.247	5.01	342.853	1.841
$x = 2.0$	7.809	−1.276	4.89	359.949	1.906
$x = 2.5$	7.767	−1.420	4.40	356.173	1.835
$x = 5.0$	7.745	−1.455	4.29	308.013	1.967

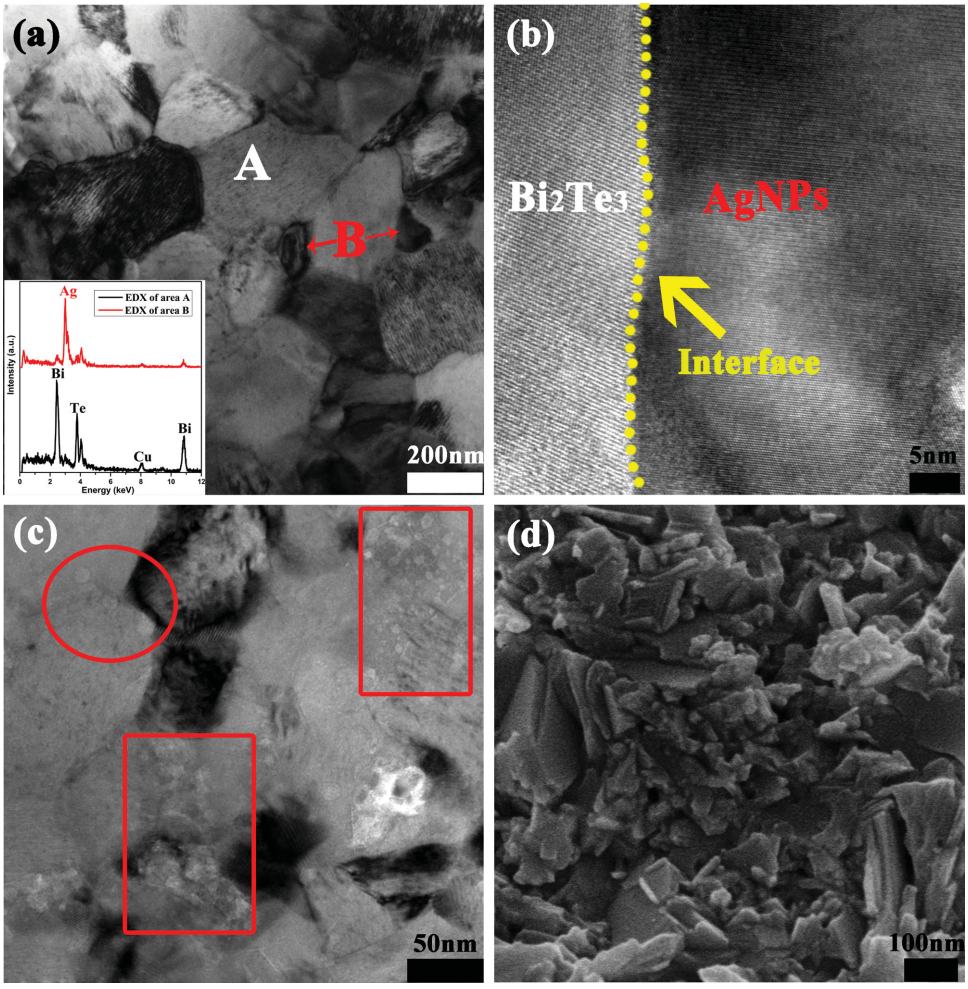

Figure 4. All images were obtained from bulk Bi_2Te_3 sample with 5.0 vol.% AgNPs. a) Low-magnification TEM image of the bulk nanocomposites. b) HR-TEM image showing the newly-built interface between the Bi_2Te_3 matrix and AgNPs. c) TEM image showing the fine Bi_2Te_3 precipitates. d) Enlarged FE-SEM image of the fractured surface.

at grain boundaries could promote electrical connectivity to improve electronic transport.[23] Since the electrical conductivity can be calculated by $\sigma = ne\mu$, where n is the carrier concentration, e is the electron charge, and μ is the carrier mobility,[6] we measured Hall coefficient (R_H) at room temperature on a PPMS system in order to elucidate the behavior of σ. Assuming parabolic bands and a single-band conduction process at 300 K, we calculated the carrier concentration (n_H) and Hall mobility (μ_H) from the measured R_H and σ using the relationn $n_H = -1/eR_H$ and $\mu_H = \sigma R_H$, respectively, where e is the free electron charge (1.602×10^{-19} C). As shown in Table 1, the Hall coefficients are all negative, indicating n-type electrical transport property. It should be pointed out that as the AgNPs content increases, the Hall mobility generally presents a declining trend, and the carrier concentration rises first and then falls. But all AgNPs-dispersed Bi_2Te_3 bulk samples have higher carrier concentration than that of single-phase bulk Bi_2Te_3. As is reported, Ag nanoparticles of size smaller than 35 nm may be molten at 350 °C.[37] The raised carrier concentration due to the introduction of AgNPs is likely a consequence of AgNPs with small size and high activity going to the interstitial site of Bi_2Te_3. Even so, there is a limitation to diffusion between Ag and Bi_2Te_3, and in this work, Ag nanoparticles have a mean diameter of 60 nm, so an overwhelming majority of Ag remains metal nanoinclusions embedded between the grain boundaries, as seen in Figure 4a. And that's exactly what reduces the Bi_2Te_3 grains and forms new interfaces and defects to enhance carrier scattering and decrease carrier mobility (as shown in Table 1), giving rise to a decrease in electrical conductivity at high Ag content. Therefore, the variation of σ values for composites could be attributed to the combination of the change of carrier concentration and the reduction of carrier mobility that occur on account of different levels of a second nanophase.

Figure 5b shows the temperature dependence of α for Bi_2Te_3 bulk samples with differernt AgNPs contents. The values of α for all samples are negative, indicative of n-type electrical transport property and in agreement with the Hall coefficient measurements. The results clearly show that the absolute α values for single-phase bulk Bi_2Te_3 fall steeply with increasing temperature, but after the dispersion of AgNPs, the α values are found to increase with temperature in the range of 300–420 K, as is similar to the trend observed in the Cu-decorated $Bi_{0.5}Sb_{1.5}Te_3$

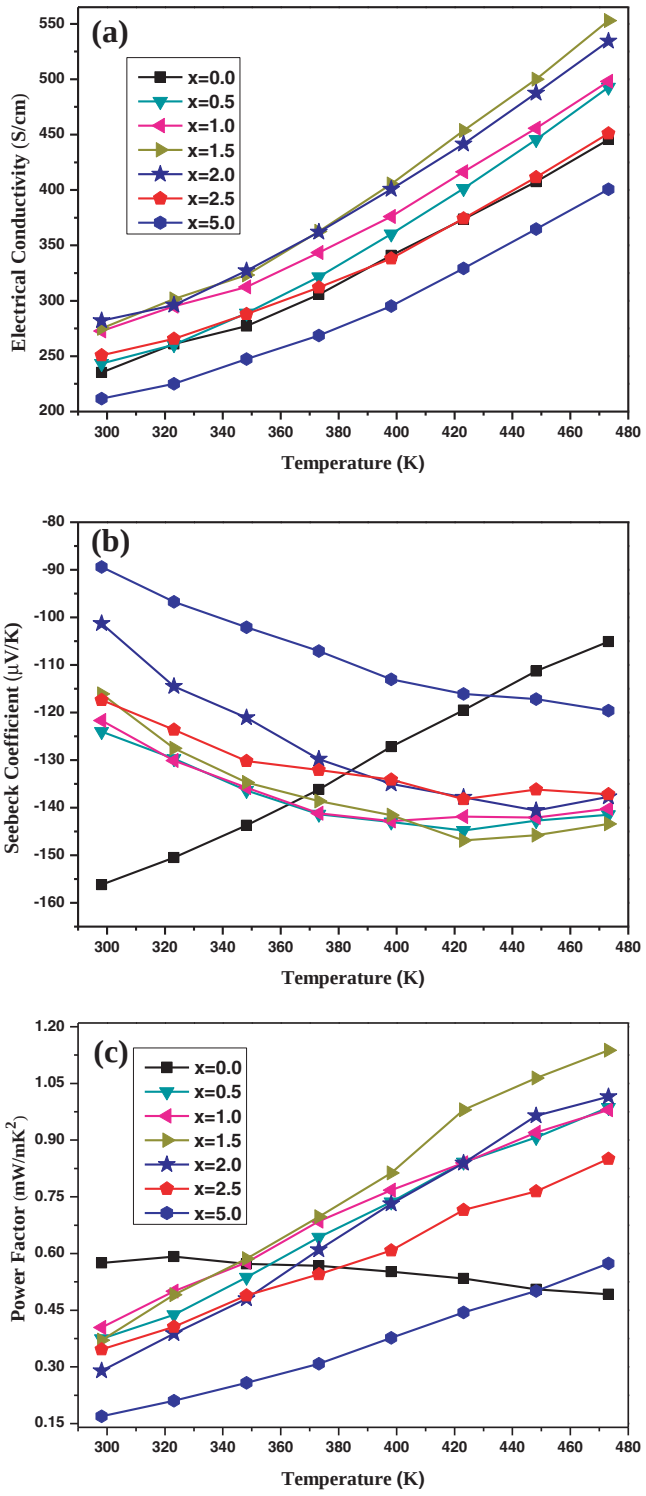

Figure 5. Temperature-dependence of a) electrical conductivity, b) Seebeck coefficient, and c) power factors for Bi_2Te_3 bulk samples with *x* vol% AgNPs contents (*x* = 0.0, 0.5, 1.0, 1.5, 2.0, 2.5, 5.0).

nanocomposite.[18] In addition, the absolute values of α decreases gradually with increasing AgNPs content at low temperatures. A minimum value of −89.4 μV K^{-1} at room temperature has been obtained when the AgNPs content is 5.0 vol%, which is much lower than that of single-phase bulk Bi_2Te_3 (−156.2 μV K^{-1}). On the basis of a degenerate parabolic band semiconductor model, the Seebeck coefficient can be calculated by

$$\alpha = \frac{8\pi^2 k_B^2}{3eh^2} m^* T \left(\frac{\pi}{3n}\right)^{2/3} \quad (1)$$

where k_B, h, m^*, and n are Boltzmann constant, Planck constant, effective mass of carrier, and carrier concentration, respectively.[6,18,48] Since the carrier concentration first increases and then decreases with increasing AgNPs content at 300 K, yet the absolute Seebeck coefficient is gradually reduced, we speculate that the decrease of α at low temperature for AgNPs-dispersed composites should not be merely attributed to the the carrier concentration, but also result from the variation in effective mass of carrier. However, at the higher temperatures, AgNPs-dispersed Bi_2Te_3 composites possess higher Seebeck coefficients, which is considered to be caused by the carrier-filtering effect.[14,19,49] Band bending at the interfaces between the Ag nanoinclusions and the matrix produces a potential barrier, resulting in the strong energy dependence of the carrier relaxation times $\tau(E)$ from different work function, which preferentially scatters the charge carriers with lower energy, as is illustrated in **Figure 6**.

The power factors ($\alpha^2\sigma$) of all samples calculated from the Seebeck coefficients and electrical conductivities are shown in Figure 5c. At lower temperatures, the values of $\alpha^2\sigma$ for single-phase bulk Bi_2Te_3 are a little higher than those of the samples with different content AgNPs due to the decrease of Seebeck coefficients. Nevertheless, the dispersion of AgNPs apparently increases the power factor at higher temperatures, reaching a maximum of 1.14 mWm^{-1} K^{-2} when the addition is 1.5 vol%. This value is an approximately 133% improvement compared with that of the AgNPs-free sample (0.49 mWm^{-1} K^{-2}), which is attributed to the combination of increased electrical conductivity and improved Seebeck coefficient. It should be noted that one of the well-known drawbacks of low-temperature chemical synthesis is the material instability at high temperatures. In order to examine the material stability at high temperatures,

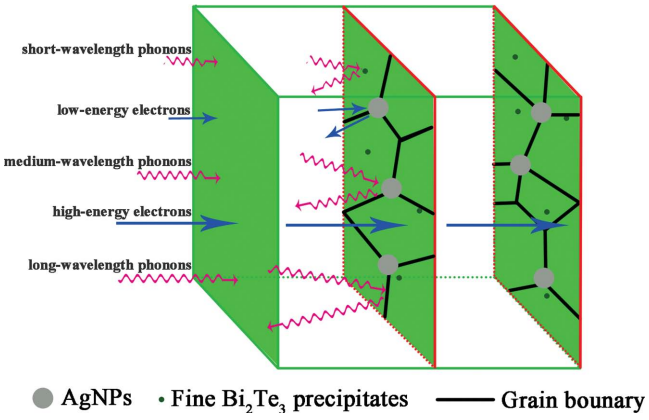

Figure 6. Schematic drawing of a hierarchical two-phased heterostructure shows the strong scattering of phonons with multiscale mean free paths along with the energy filtering effect.

we have retested the Seebeck coefficient and electrical conductivity of some samples up to 523 K for multiple times. New test results (see Figure S1, Supporting Information) are basically consistent with the original ones, and the power factors exhibit slightly increasing trend at high temperatures (480–523 K). The samples prepared by low-temperature synthesis in our work have showed good stability and reproducibility at temperatures up to 523 K.

Figure 7a shows the total thermal conductivity (κ_{tot}) of bulk Bi_2Te_3 samples with differernt content of AgNPs as a function of temperature. As expected, the dispersion of AgNPs significantly reduces κ_{tot} in the whole measured temperature range. The minimum value reaches as low as 0.41 Wm^{-1} K^{-1} for bulk Bi_2Te_3 with 2.0 vol% AgNPs at room temperature, which is much lower than that of pristine bulk Bi_2Te_3 (0.77 Wm^{-1} K^{-1}). Since the total thermal conductivity consists of carrier thermal conductivity (κ_{car}), lattice thermal conductivity (κ_{lat}), and bipolar thermal conductivity (κ_{bipo}), and κ_{bipo} is usually negligible near room temperature, κ_{lat} is therefore obtained by directly subtracting κ_{car} from κ_{tot}.[45,50] On the basis of the Wiedemann–Franz law, the κ_{car} is roughly calculated by the relation $\kappa_{car} = L_0\sigma T$, where L_0 is the Lorentz number, varying from 1.5×10^{-8} V^2 K^{-2} for nondegenerated semiconductors to 2.44×10^{-8} V^2 K^{-2} for strongly degenerated semiconductors.[51,52] Here, the Lorenz number was obtained by applying the Fermi–Dirac statistics as follows

$$L_0 = \left(\frac{k_B}{e}\right)^2 \left(\frac{(r+7/2)F_{(r+5/2)}(\eta)}{(r+3/2)F_{(r+1/2)}(\eta)} - \left[\frac{(r+5/2)F_{(r+3/2)}(\eta)}{(r+3/2)F_{(r+1/2)}(\eta)}\right]^2 \right) \quad (2)$$

assuming scattering factor $r = -1/2$. The reduced Fermi energy (η) used in the above calculations could be derived from the experimental data of the absolute Seebeck coefficientby using the following relationship[53–56]

$$S = \pm \frac{k_B}{e}\left(\frac{(r+5/2)F_{(r+3/2)}(\eta)}{(r+3/2)F_{(r+1/2)}(\eta)} - \eta \right) \quad (3)$$

$$F_n(\eta) = \int_0^\infty \frac{\chi^n}{1+e^{\chi-\eta}}\, d\chi \quad (4)$$

$$\eta = \frac{E_f}{k_B T} \quad (5)$$

where E_f is the Fermi energy. On the basis of the above calculation for Lorenz number (shown in Table 1), the temperature-dependent κ_{car} and κ_{lat} of all samples are obtained and shown in Figure 7b,c. It can be seen that all AgNPs-dispersed Bi_2Te_3 bulk samples have lower κ_{lat} than that of single-phase bulk Bi_2Te_3 at identical measuring temperature, while κ_{car} exhibits little change as the AgNPs content increases. Therefore, as we expect, the κ_{lat} makes major contributions to the κ_{tot}. As schematically shown in Figure 6, the remarkable reduction in lattice thermal conductivity with increasing Ag additions is thought to be caused by strong scattering of phonons with multiscale

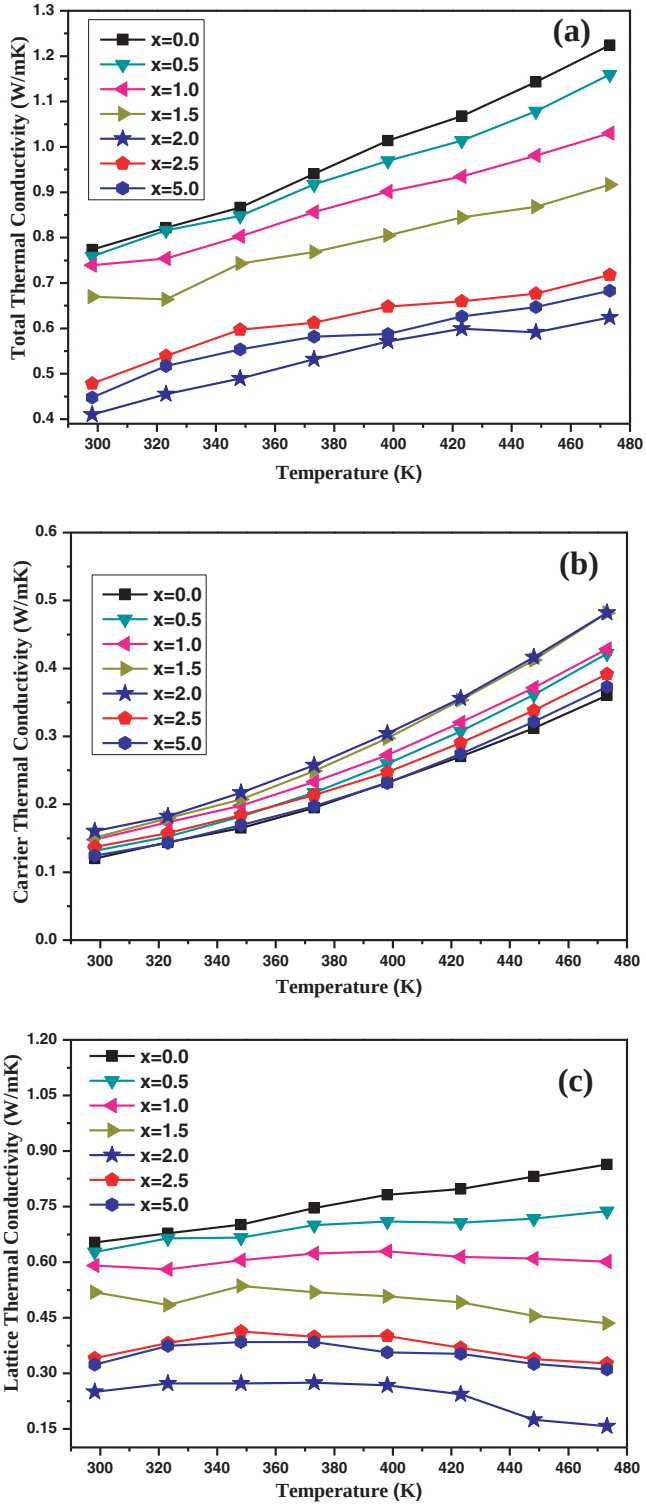

Figure 7. Temperature-dependence of a) total thermal conductivity, b) carrier thermal conductivity, c) lattice thermal conductivity for Bi_2Te_3 bulk samples with *x* vol% AgNPs contents (*x* = 0.0, 0.5, 1.0, 1.5, 2.0, 2.5, 5.0).

mean free paths: (a) multiscale nanostructure that derives from the dispersion of AgNPs based on the combination of solution-based synthesis with SPS technique, effectively scattering

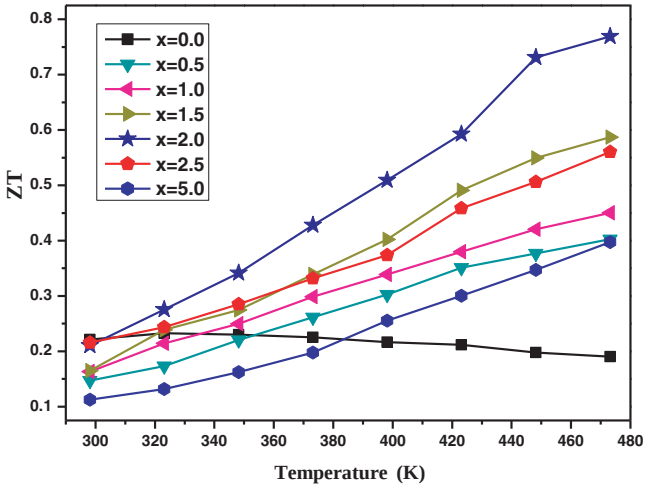

Figure 8. Temperature-dependence of ZT values for Bi_2Te_3 bulk samples with *x* vol% AgNPs contents (*x* = 0.0, 0.5, 1.0, 1.5, 2.0, 2.5, 5.0).

phonons with short and medium mean free paths (3–100 nm); (b) further scattering of the phonons with longer mean free paths (0.1–1 μm) due to the rough newly formed interfaces along with the increased grain boundaries on account of the grain size reduction; (c) additional strong short-wavelength phonons scattering resulting from fine nano-precipitates or point defects.[20,22,31] Furthermore, it is worth noting that the lowest thermal conductivity has been obtained by adding 2.0 vol% AgNPs instead of 5.0 vol%. Therefore, the observed reduction in thermal conductivity is not simply attributed to a disruption of the Bi_2Te_3 matrix caused by introducing more and more of a second phase, but achieved provided that the nanosized second phase is chosen judiciously to cause increased phonon scattering, which is present at an optimum (not maximum) concentration.[43,57] In addition, it should be pointed out that the Lorenz number which depends on the scattering parameter and the reduced Fermi energy may not be constant for all samples. As is reported, the Lorenz number shows an increasing trend with doping level, indicating there may be more decrease in the κ_{lat} as the AgNPs content increases.[56,58]

The dimensionless thermoelectric figures of merit ZT of all bulk samples are calculated from the relation $ZT = \alpha^2\sigma T/\kappa$ and the results are shown in **Figure 8**. It is found that the ZT values for all AgNPs-despersed bulk samples increase with the increasing temperature, which is different from the variation trend of single-phase bulk Bi_2Te_3. Furthermore, the dispersioon of Ag nanoparticles leads to a remarkable increase in ZT, reaching a maximum ZT value of 0.77 at 475 K from the bulk Bi_2Te_3 dispersed with 2.0 vol% AgNPs, approximately three times higher than that of the Bi_2Te_3 matrix. The results indicate that the dispersion of AgNPs can lead to significant enhancement of thermoelectric performance for Bi_2Te_3-based materials over the whole temperature range given that the AgNPs content is controlled properly. The improvement in ZT of AgNPs-dispersed Bi_2Te_3 is mainly attributed to three factors: (i) the grain growth inhibition, resulting in a higher density of multiscale grains to increase scattering of phonon with short and medium mean free paths; (ii) numerous newly formed interfaces/boundaries, nanoscale precipitates, and point-defects scattering, causing intense scattering of both long-wavelength and short-wavelength phonons, and therefore significantly reducing the lattice thermal conductivity; (iii) a contact potential difference between the phase interfaces due to a different work function between AgNPs and Bi_2Te_3 matrix, scattering low-energy electrons to improve the Seebeck coefficient. We have to admit that the ZT values have not exceeded 1.0 in this work, mainly owing to the low performance of our Bi_2Te_3 parent that is synthesized by a surfactant-mediated hydrothermal method, which needs to be modified by further optimizations. Neverthless, the improvement range due to the dispersion of AgNPs has been hardly achieved in previous reports. Therefore, we assure that the ZT values could be much higher if the properties of thermoelectric matrix are enhanced.

3. Conclusion

The AgNPs-dispersed Bi_2Te_3 nanocomposite thermoelectric materials were prepared by a solution-based ultrasonic-dispersion method and subsequent spark plasma sintering technique. It is found that Ag nanoparticles that are uniformly dispersed on the grain boundaries not only effectively suppress the Bi_2Te_3 grains growth, but also create numerous new interfaces and defects, forming a hierarchical two-phased heterostructure within the matrix. The hierarchical heterostructure within the AgNPs/Bi_2Te_3 thermoelectric composites causes strong scattering of phonons across integrated length scales, significantly reducing the lattice thermal conductivity. Meanwhlie, the newly formed interfaces and defects distinctly enhance the Seebeck coefficients at high temperatures thanks to the carrier-filtering effect, in spite of the inevitably enhanced carrier scattering leading to a slight decrease in carrier mobility. Compared with single-phase Bi_2Te_3, the samples dispersed with AgNPs exhibited the much lower thermal conductivity and higher power factor. Consequently, a maximum ZT value of 0.77 was obtained at 475 K from the bulk Bi_2Te_3 dispersed with 2.0 vol% AgNPs, approximately three times higher than that of the pristine bulk Bi_2Te_3. Therefore, our route to construct thermoelectric nanocomposites with hierarchical heterostructure turns out to be effective and feasible. Actually, we have also triumphantly improved thermoelectric performance of other matrix by dispersing AgNPs through this route and the results will be reported in future publications. Furthermore, we here attribute the simultaneous increases of electrical conductivity and Seebeck coefficient with increasing temperature to the electron energy filtering effect, on which theoretical transport calculations will be done in the following work to fit the temperature-dependent properties with an estimated barrier height for validation purposes. We assure that constructing hierarchical two-phased heterostructure in TE materisls is a promising way to significantly improve ZT values and our route is meaningful for mass production of nanocomposite TE materisls for potential industrial applications.

4. Experimental Section

All chemicals were obtained from Sinopharm Chemical Reagent Co., Ltd and used as received without further purification.

Preparation: The Bi_2Te_3 nanopowders and AgNPs were separately synthesized in this work. Bi_2Te_3 was prepared by a typical surfactant-mediated hydrothermal method identical with our previous report.[43] AgNPs in sufficient quantities for integration into the Bi_2Te_3 nanopowders were prepared by using polyol reduction of silver nitrate according to the reference with a slight modification.[39] For the synthesis of the AgNPs, ethylene glycol (EG, AR, 60 mL) was added into a 250 mL three-necked round flask and heated in an oil bath at 150 °C under magnetic stirring with a large, egg-shaped Teflon-coated stir bar. After preheating for 50 min, a flow of argon was introduced to vent atmosphere via a glass pipet at a flow rate of 1200 mL min^{-1} and delivered throughout the whole reaction process. One mouth of the reaction flask was capped by a perforated glass stopper to allow the gaseous species to escape. 10 min later, 0.7 mL of a sodium sulfide (Na_2S, AR) solution in EG (3×10^{-3} M) was quickly injected into the preheated EG solution, followed by injecting 15 mL of a poly(vinylpyrrolidone) (PVP, K-30) solution in EG (20 mg mL^{-1}) and 8 min later 5 mL of a silver nitrate ($AgNO_3$, AR) solution in EG (48 mg mL^{-1}). The solution was then heated for 20 min under magnetic stirring at a rate of 300 rpm till the final color shifted to green ocher, which indicated the formation of AgNPs. After natural cooling to room temperature, the resultant products were washed with acetone, followed by deionized water to remove excess EG and PVP. During washing process, the suspension was centrifuged at 6000 rpm for 30 min and then the supernatant was removed by a pipet. Finally, the AgNPs were dispersed in deionized water for storage and some were dried in vacuum at 50 °C for calculating the yield and further characterization. After converting volume ratio into mass ratio, the synthesized AgNPs were introduced into the Bi_2Te_3 powders matrix at different proportion and then dispersed homogeneously in absolute ethyl alcohol through ultrasound and stirring for 5 h. The final products were successively centrifuged at 9000 rpm for 30 min, washed with deionized water, absolute ethyl alcohol for several times, and finally dried in vacuum at 50 °C. The as-prepared AgNPs-dispersed Bi_2Te_3 composite powders were consolidated by using a spark plasma sintering (SPS, Dr. Sinter 725, Japan) technique. The nanopowders were loaded into cylindrical carbon dies with an inner diameter of 10 mm and then sintered at a heating rate of 70 °C min^{-1} and starting pressure of 30 MPa in an argon environment. The final sintering parameters were selected as 350 °C, 80 MPa and a dwelling time of 6 min.

Characterization: Phase structures for all powders and bulk nanocomposites were characterized by X-ray diffraction (XRD, Rigaku D/Max-2550 PC, Japan) with Cu Ka radiation at 40 kV, 200 mA. The UV–vis absorption spectra were taken at the room temperature on a LanbdaA35 spectrometer (USA) using a quartz cuvette after the solution was diluted 30× with deionized water. Microstructures for powders and the fractured surfaces of bulk AgNPs-dispersed Bi_2Te_3 composite were investigated by a field emission scanning electron microscope (FESEM, S-4800, Japan). The TEM specimen for AgNPs was prepared by placing small droplets of the diluted (by 100× with deionized water) reaction solutions on copper grids and then characterized by a transmission electron microscopy (TEM, Model 2100F, Japan) with a selected area electron diffraction (SAED). The AgNPs within the bulk Bi_2Te_3 matrix were determined by HR-TEM (TECNAI G^2S) and energy dispersive X-ray (EDX) patterns. The thermoelectric properties of all bulk samples were measured in the temperature range of 300–475 K. The thermal conductivity (κ) was calculated by combining thermal diffusivity, specific heat with sample density according to $\kappa = a \times C_p \times \rho$. The thermal diffusivity (a) was measured by a laser flash apparatus, Netzsch LFA 427 (Selb, Germany) and the specific heat (C_p) was tested by a differential scanning calorimeter (DSC, Netzsch 204F1). Densities were measured by an Archimedes method. The Seebeck coefficient and electrical conductivity were simultaneously measured by the standard four-probe methods under a helium atmosphere using a ZEM-3 equipment (ULVAC–RIKO, Japan) after samples were cut into rectangles of about 2 mm × 2 mm × 8 mm. The room-temperature Hall coefficient (R_H) measurements were performed on a PPMS system (Quantum Design INC., USA) with a magnetic field of 2 T and an electrical current of 30 mA.

Supporting Information

Supporting Information is available from the Wiley Online Library or from the author.

Acknowledgements

This work was funded by Natural Science Foundation of China (Grant Nos. 51374078 and 51432004), Shanghai Committee of Science and Technology (Grant Nos. 13JC1400100 and 13NM1400101), "Shu Guang" project supported by Shanghai Municipal Education Commission and Shanghai Education Development Foundation (Grant Nos. 11SG34), PCSIRT (Grant No. IRT1221), the Fundamental Research Funds for the Central Universities, and DHU Distinguished Young Professor Program.

Received: August 6, 2014
Revised: November 6, 2014
Published online: December 28, 2014

[1] R. Venkatasubramanian, E. Siivola, T. Colpitts, B. O'Quinn, *Nature* **2001**, *413*, 597.
[2] C. Han, Z. Li, S. X. Dou, *Chin. Sci. Bull.* **2014**, *59*, 2073.
[3] T. M. Tritt, *Science* **1999**, *283*, 804.
[4] B. C. Sales, *Science* **2002**, *295*, 1248.
[5] L. D. Hicks, M. S. Dresselhaus, *Phys. Rev. B* **1993**, *47*, 2727.
[6] G. J. Snyder, E. S. Toberer, *Nat. Mater.* **2008**, *7*, 105.
[7] C. J. Vineis, A. Shakouri, A. Majumdar, M. G. Kanatzidis, *Adv. Mater.* **2010**, *22*, 3970.
[8] Y. C. Lan, A. J. Minnich, G. Chen, Z. F. Ren, *Adv. Funct. Mater.* **2010**, *20*, 357.
[9] J. F. Li, W. S. Liu, L. D. Zhao, M. Zhou, *NPG Asia Mater.* **2010**, *2*, 152.
[10] W. S. Liu, X. Yan, G. Chen, Z. F. Ren, *Nano Energy* **2012**, *1*, 42.
[11] H. Alam, S. Ramakrishna, *Nano Energy* **2013**, *2*, 190.
[12] B. Poudel, Q. Hao, Y. Ma, Y. Lan, A. Minnich, B. Yu, X. Yan, D. Wang, A. Muto, D. Vashaee, X. Chen, J. Liu, M. S. Dresslhaus, G. Chen, Z. Ren, *Science* **2008**, *320*, 634.
[13] W. J. Xie, J. He, H. J. Kang, X. F. Tang, S. Zhu, M. Laver, S. Y. Wang, J. R. D. Copley, C. M. Brown, Q. J. Zhang, T. M. Tritt, *Nano Lett.* **2010**, *10*, 3283.
[14] S. V. Faleev, F. Leonard, *Phys. Rev. B* **2008**, *77*, 214304.
[15] M. Zebarjadi, K. Esfarjani, A. Shakouri, J. H. Bahk, Z. X. Bian, G. Zeng, J. Bowers, H. Lu, J. Zide, A. Gossard, *Appl. Phys. Lett.* **2009**, *94*, 202105.
[16] Y. Ma, R. Heijl, A. E. C. Palmqvist, *J. Mater. Sci.* **2013**, *48*, 2767.
[17] Y. C. Zhang, G. D. Stucky, *Chem. Mater.* **2014**, *26*, 837.
[18] K. H. Lee, H. S. Kim, S. I. Kim, E. S. Lee, S. M. Lee, J. S. Rhyee, J. Y. Jung, I. H. Kim, Y. Wang, K. Koumoto, *J. Electron. Mater.* **2012**, *41*, 1165.
[19] S. Hwang, S. Kim, K. Ahn, J. W. Roh, D. J. Yang, S. M. Lee, K. H. Lee, *J. Electron. Mater.* **2013**, *42*, 1411.
[20] S. Y. Wang, H. Li, R. M. Lu, G. Zheng, X. F. Tang, *Nanotechnology* **2013**, *24*, 285702.
[21] J. H. Li, Q. Tan, J. F. Li, D. W. Liu, F. Li, Z. Y. Li, M. M. Zou, K. Wang, *Adv. Funct. Mater.* **2013**, *23*, 4317.
[22] S. Sumithra, N. J. Takas, D. K. Misra, W. M. Nolting, P. F. Poudeu, K. L. Stokes, *Adv. Energy Mater.* **2011**, *1*, 1141.
[23] X. Y. Zhou, G. Y. Wang, L. Zhang, H. Chi, X. L. Su, J. Sakamoto, C. Uher, *J. Mater. Chem.* **2012**, *22*, 2958.
[24] Y. Z. Pei, J. L. Falk, E. S. Toberer, D. L. Medlin, G. J. Snyder, *Adv. Funct. Mater.* **2011**, *21*, 241.
[25] K. Park, J. S. Son, S. Woo, K. Shin, M. W. Oh, S. D. Park, T. Hyeon, *J. Mater. Chem. A* **2014**, *2*, 4217.

[26] S. H. Lo, J. Q. He, K. Biswas, M. G. Kanatzidis, V. P. Dravid, *Adv. Funct. Mater.* **2012**, *22*, 5175.
[27] Y. C. Zhang, H. Wang, S. Kraemer, Y. F. Shi, F. Zhang, M. Snedaker, K. Ding, M. Moskovits, G. J. Snyder, G. D. Stucky, *ACS Nano* **2011**, *5*, 3158.
[28] D. Jung, K. Kurosaki, S. Seino, M. Ishimaru, K. Sato, Y. J. Ohishi, H. Muta, S. Yamanaka, *Phys. Status Solidi B* **2014**, *251*, 162.
[29] S. F. Fan, J. N. Zhao, Q. Y. Yan, J. Ma, H. H. Hng, *J. Electron. Mater.* **2011**, *40*, 1018.
[30] Z. He, C. Stiewe, D. Platzek, G. Karpinski, E. Muller, *J. Appl. Phys.* **2007**, *101*, 043707.
[31] K. Biswas, J. Q. He, I. D. Blum, C. Wu, T. P. Hogan, D. N. Seidman, V. P. Dravid, M. G. Kanatzidis, *Nature* **2012**, *489*, 414.
[32] C. Dames, G. Chen, *Thermoelectrics Handbook: Macro to Nano*, Taylor & Francis, Boca Raton, FL **2006**.
[33] K. Esfarjani, G. Chen, H. T. Stokes, *Phys. Rev. B* **2011**, *84*, 085204.
[34] B. Qiu, H. Bao, G. Q. Zhang, Y. Wu, X. L. Ruan, *Comput. Mater. Sci.* **2012**, *53*, 278.
[35] Z. T. Tian, J. Garg, K. Esfarjani, T. Shiga, J. Shiomi, G. Chen, *Phys. Rev. B* **2012**, *85*, 184303.
[36] M. Zebarjadi, J. Yang, K. Lukas, B. Kozinsky, B. Yu, M. S. Dresselhaus, C. Opeil, Z. F. Ren, G. Chen, *J. Appl. Phys.* **2012**, *112*, 044305.
[37] O. A. Yeshchenko, I. M. Dmitruk, A. A. Alexeenko, A. V. Kotko, *Nanotechnology* **2010**, *21*, 045203.
[38] Y. G. Sun, Y. D. Yin, B. T. Mayers, T. Herricks, Y. N. Xia, *Chem. Mater.* **2002**, *14*, 4736.
[39] Q. Zhang, C. Cobley, L. Au, M. McKiernan, A. Schwartz, L. P. Wen, J. Y. Chen, Y. N. Xia, *ACS Appl. Mater. Interfaces* **2009**, *1*, 2044.
[40] M. Scheele, N. Oeschler, K. Meier, A. Kornowski, C. Klinke, H. Weller, *Adv. Funct. Mater.* **2009**, *19*, 3476.
[41] M. Zebarjadi, K. Esfarjani, Z. X. Bian, A. Shakouri, *Nano Lett.* **2011**, *11*, 225.
[42] F. Li, T. R. Wei, F. Y. Kang, J. F. Li, *J. Mater. Chem. A* **2013**, *1*, 11942.
[43] Q. H. Zhang, X. Ai, W. J. Wang, L. J. Wang, W. Jiang, *Acta Mater.* **2014**, *73*, 37.
[44] A. I. Hochbaum, R. K. Chen, R. D. Delgado, W. J. Liang, E. C. Garnet, M. Najarian, A. Majumdar, P. D. Yang, *Nature* **2008**, *451*, 163.
[45] K. T. Kim, S. Y. Choi, E. H. Shin, K. S. Moon, H. Y. Koo, G. G. Lee, G. H. Ha, *Carbon* **2013**, *52*, 541.
[46] J. S. Son, M. K. Choi, M. K. Han, K. Park, J. Y. Kim, S. J. Lim, M. Oh, Y. Kuk, C. Park, S. J. Kim, T. Hyeon, *Nano Lett.* **2012**, *12*, 640.
[47] Y. L. Pei, H. J. Wu, J. H. Sui, J. Li, D. Berardan, C. Barreteau, L. Pan, N. Dragoe, W. S. Liu, J. Q. He, L. D. Zhao, *Energy Environ. Sci.* **2013**, *6*, 1750.
[48] S. N. Guin, D. S. Negi, R. Datta, K. Biswas, *J. Mater. Chem. A* **2014**, *2*, 4324.
[49] J. Y. Peng, L. W. Fu, Q. Z. Liu, M. Liu, J. Y. Yang, D. Hitchcock, M. H. Zhou, J. He, *J. Mater. Chem. A* **2014**, *2*, 73.
[50] S. Chen, K. C. Lukas, W. S. Liu, C. P. Opeil, G. Chen, Z. F. Ren, *Adv. Energy Mater.* **2013**, *3*, 1210.
[51] K. T. Wojciechowski, M. Schmidt, *Phys. Rev. B* **2009**, *79*, 184202.
[52] L. D. Zhao, J. Q. He, C. I. Wu, T. P. Hogan, X. Y. Zhou, C. Uher, V. P. Dravid, M. G. Kanatzidis, *J. Am. Chem. Soc.* **2012**, *134*, 7902.
[53] S. Johnsen, J. Q. He, J. Androulakis, V. P. Dravid, I. Todorov, D. Y. Chung, M. G. Kanatzidis, *J. Am. Chem. Soc.* **2011**, *133*, 3460.
[54] S. Ganguly, C. Zhou, D. Morelli, J. Sakamoto, C. Uher, S. L. Brock, *J. Solid State Chem.* **2011**, *184*, 3195.
[55] S. N. Girard, Jiaqing He, X. Y. Zhou, D. Shoemaker, C. M. Jaworski, C. Uher, V. P. Dravid, J. P. Heremans, M. G. Kanatzidis, *J. Am. Chem. Soc.* **2011**, *133*, 16588.
[56] L. D. Zhao, S. H. Lo, J. Q. He, H. Li, K. Biswas, J. Androulakis, C. Wu, T. P. Hogan, D. Y. Chung, V. P. Dravid, M. G. Kanatzidis, *J. Am. Chem. Soc.* **2011**, *133*, 20476.
[57] J. R. Sootsman, R. J. Pcionek, H. J. Kong, C. Uher, M. G. Kanatzidis, *Chem. Mater.* **2006**, *18*, 4993.
[58] W. S. Liu, Q. Y. Zhang, Y. C. Lan, S. Chen, X. Yan, Q. Zhang, H. Wang, D. Z. Wang, G. Chen, Z. F. Ren, *Adv. Energy Mater.* **2011**, *1*, 577.